Probing strain in wurtzite InP-InAs core-shell nanowires with Raman spectroscopy

Yongqian Zhao,[1,2] Mengfei Xue,[1,2] D. J. O. Göransson,[3] M. T. Borgström,[3] H. Q. Xu,[3,4,5,*] and Jianing Chen[1,2,6,†]

[1]*Beijing National Laboratory for Condensed Matter Physics, Institute of Physics, Chinese Academy of Sciences Beijing, 100190, China*

[2]*School of Physical Sciences, University of Chinese Academy of Sciences, Beijing 100049, China*

[3]*NanoLund and Division of Solid State Physics, Lund University, Box 118, S-22100 Lund, Sweden*

[4]*Beijing Key Laboratory of Quantum Devices, Key Laboratory for Physics and Chemistry of Nanodevices and Department of Electronics, Peking University, Beijing 100190, China*

[5]*Beijing Academy of Quantum Information Sciences, Beijing 100193, China*

[6]*Songshan Lake Materials Laboratory, Dongguan, Guangdong 523808, China*

(Received 10 July 2021; revised 29 October 2021; accepted 14 December 2021; published 30 December 2021)

We used Raman spectroscopy to investigate phonon modes of single InP-InAs core-shell nanowire with a pure wurtzite phase to reveal the embedded strained state. Raman spectra show that the InP core exhibits tensile strain and the InAs shell exhibits compressive strain due to the radial heterostructure growth. Using different polarization excitation configurations, we identified distinct A_1 (TO) and E_1 (TO) modes, atomic vibrations along and perpendicular to the [0001] direction, respectively. We also identified E_{2h} phonon modes in wurtzite InP and InAs, lattice vibration along with the [0001] direction, a fingerprint to distinguish a wurtzite phase from a zinc-blende phase. The Raman spectra changes reveal the resonance effects of InP and InAs between the $E_0 + \Delta_0$ energy level and the E_1 gap by varying excitation energy, which indicates Γ_{7c}-Γ_{6v} transition consists of a split-off valence band and a band-gap transition along [0001] directions of the Brillouin zone. The polar patterns show the Raman A_1 (TO) mode of InP only predominates in the $x(yy)\bar{x}$ configuration, indicating the InP A_1 (TO) phonon is sensitive to excitation polarization, suggesting the resonant Raman spectroscopy with specific polarization offers a direct way for characterizing wurtzite InP. Our findings deepen the understanding of strain in wurtzite-phase core-shell nanowire, providing a significant reference for engineering strain in core-shell nanowire to control optical and electric properties.

DOI: 10.1103/PhysRevB.104.235309

I. INTRODUCTION

In recent years, semiconductor nanowires (NWs) have attracted great interest due to their intriguing potential in the new generation of optoelectronic nanoscale devices [1–4]. Compared to the bulk materials, NWs show novel properties since materials' physical properties depend on their size. The flexibility of NWs in designing both radial and axial heterostructures provides excellent promise for applications in photodetectors [5,6], waveguides [7,8], single-photon emitters [9,10], and light-emitting diodes [11,12]. Core-shell NWs, especially the InP-InAs core-shell NWs, have been reporting intriguing optical [13–15] and electrical [16,17] properties such as improved electron mobility [17] and emitting at telecommunication wavelengths [14] since the sizable surface-to-volume ratio allows them to accommodate more strain between the core and the shell beyond restrictions set by the lattice matching in two-dimensional epitaxial films. The strain in core-shell NWs arises from the lattice mismatch between core, shell, and the geometrical shape of the cross section of NWs [18,19]. Therefore, the convenience of designing core-shell NWs has attracted considerable interest in exploring their novel physical properties for optoelectrical applications. A great deal of research has been conducted on NW arrays; however, the morphology uniformity, doping, defects, and other factors of NWs are still not apparent. The overall average property of the array does not represent the property of a single NW. Still, the property of a single NW and its uniformity will significantly affect the entire array's performance. Therefore, the study of a single NW property holds guiding significance for improving the overall performance of the NW array and promoting its application in optoelectronic devices.

The band structure of the wurtzite phase differs significantly from the zinc-blende phase in a semiconductor material [20]. In bulk form, most non-nitride III–V materials are stable only in the zinc-blende phase. However, NWs are stable in zinc-blende and wurtzite structures, crystallizing in [111] or [0001] direction. Raman spectroscopy is a nondestructive technique to acquire material information on the composition [21], strain [22], crystal structures, and electric states of semiconductor NWs. Comprehensive Raman spectroscopy studies of NWs on the phonon confinement [23], heating [24], and antenna effect [25] have been reported, and properties of strained radial and axial heterostructures of GaN/InN [26], InAs/GaAs [27], and InAs/InP [28] have been characterized. However, strain in single wurtzite InAs-InP core-shell NWs with polarized and resonant Raman spectroscopy study has, to our knowledge, not been investigated. In this work, we looked into the strain inside the InP core by measuring the

*Corresponding author: hqxu@pku.edu.cn

†Corresponding author: jnchen@iphy.ac.cn

 ©2021 American Physical Society

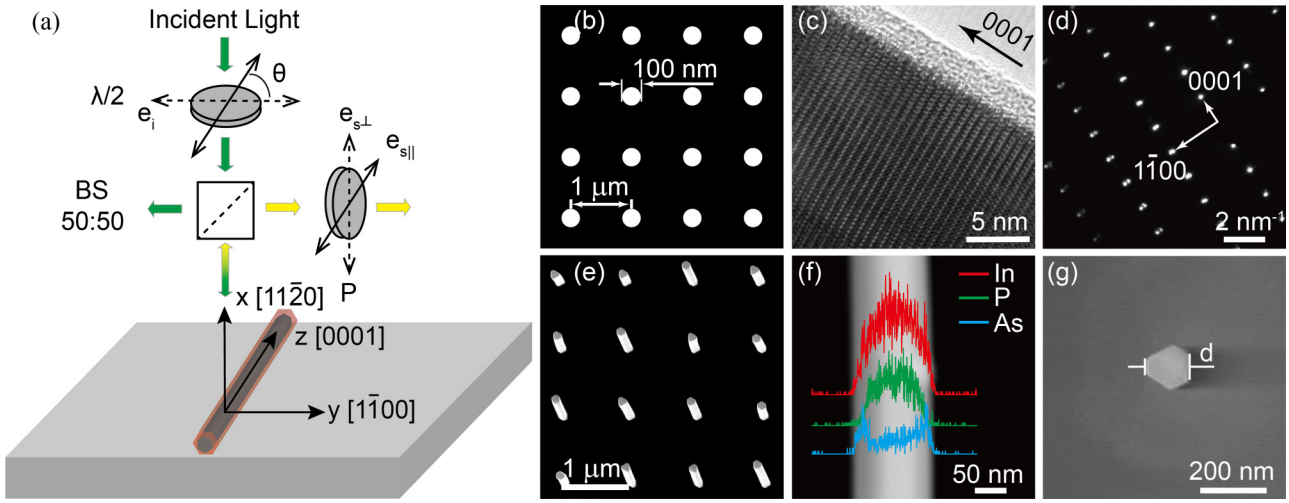

FIG. 1. (a) Sketch of the polarization configurations for InP-InAs core-shell NWs in backscattering geometry. The crystal facets of the core-shell NWs and used coordinate systems are as shown: $x = [11\bar{2}0]$, $y = [1\bar{1}00]$, $z = [0001]$. (b) Schematic diagram of shadow mask applied to grow the InP core. The diameter of the opening circle is 100 nm, and the pitch is 1 μm. (c) HRTEM image of the core-shell NWs. (d) SAED pattern of the core-shell NWs. (e) The SEM image of as-grown NWs. (f) HAADF image with line-scanned EDS of In, P, and As element across the NWs. (c), (d), (f) Viewed in the $[11\bar{2}0]$ zone axis. (g) A representative SEM image of the cross section viewed along [0001] direction from the top of a single NW; d indicates the diameter of the NW.

shift of optical phonon modes in wurtzite InP and identified different optical phonon modes of wurtzite InP and InAs. We found that the resonance effect of InP and InAs is related to the $E_0 + \Delta_0$ energy level and the E_1 gap, respectively. The InP A_1 (TO) phonon is sensitive to the polarization of excitation. Monitoring engineered strain in core-shell structures is essential for optimizing their performance on electronic and optical nanodevices applications. These findings deepen the knowledge of the band-structure tuning of the wurtzite phase InP and InAs.

II. EXPERIMENT

The InP-InAs core-shell NWs were grown by selective area metal-organic vapor phase epitaxy (MOVPE) on an InP(111A) single-crystal wafer covered with a 23-nm-thick patterned layer of SiN_x. To prepare the growth substrate, a SiN film was first deposited on the InP (111A) wafer using atomic layer deposition, and 200-nm-thick resist CSAR 62 was then spin coated onto the SiN_x cover. The resist was exposed in an electron-beam lithography system and then developed. An array of circular openings with a diameter of 100 nm [Fig. 1(b)] and a pitch of 1 μm [Fig. 1(e)] was patterned. The resist layer was utilized as an etch mask in the subsequent etching of the SiN_x cover in the openings by reactive ion etching. The diameter of the SiN openings controls the diameter of the InP core.

For synthesis, the substrate was first raised in temperature and annealed in a phosphine/H_2 atmosphere at 750 °C for 10 min. Then the molar fractions of phosphine and trimethylindium (TMIn) were set to 2.5×10^{-2} and 1.2×10^{-5}, respectively, and the temperature reduced to 710 °C, at which the InP core was grown for 10 min. TMIn was then switched off, and the temperature was lowered to 460 °C, the supply of phosphine was switched off, and the supply of arsine and TMIn was switched on with the molar fractions set to 2.1×10^{-3} and 2.0×10^{-6}, respectively, to grow the InAs shell for 4 min. Then the sample was cooled down to room temperature under an arsine/H_2 flow. The structure and composition of the NWs were characterized by using high-resolution transmission electron microscopy (HRTEM) in JEOL/JEM-2100PLUS equipped with Oxford energy-dispersive spectroscopy. Before the measurement, the NWs were mechanically transferred onto a holey carbon copper grid with the help of a fiber probe. The morphology of the cross section of the NWs was studied by scanning electron microscopy (SEM).

Raman spectroscopy was performed in a backscattering configuration under ambient conditions at room temperature using multiple excitation energy, including a HeNe laser with a wavelength of 632.8 nm, a Nd: yttrium aluminum garnet laser with a wavelength of 532 nm, and a semiconductor laser with a wavelength of 785 nm, respectively. The investigated single core-shell NWs were mechanically transferred onto a Si substrate coated with a 100-nm-thick gold film for dispersing the heat induced by laser. For positioning a single NW, the sample was laid on an XY mechanical translational stage with an accuracy of 100 nm. To study the dependence of Raman scattering on exciting polarizations, we rotated the polarization of incident light by an angle of θ to the long axis of the NWs by a $\lambda/2$ wave plate. The laser is focused on the single NW by a 100× objective of numerical aperture = 0.95, and the scattering light is collected through the same objective. The laser power was below 0.5 mW to exclude the heating effect. The laser's spot diameter is about 1 μm, which, combined with the imaging power of the microscope, enables the identification of a single NW. The polarization of scattering light e_s is selected by an analyzer, whose polarization is adjustable from perpendicular to parallel to the NWs. A schematic of the experiment setup is shown in Fig. 1(a). The z axis is set to be parallel to the [0001] direction of NWs, and the direction of the incident laser is along the x axis. For

TABLE I. Optical phonon modes and Raman polarization configurations for wurtzite InP and InAs in backscattering geometry.

Phonon modes	Polarization configurations
E_1 (TO)	$x(zy)\bar{x}$; $x(yz)\bar{x}$
A_1 (TO)	$x(zz)\bar{x}$; $x(yy)\bar{x}$
E_{2h}	$x(yy)\bar{x}$
E_1 (LO)	Forbidden
A_1 (LO)	Forbidden

convenience, Porto's notation $k_i(e_ie_s)k_s$ is adopted to denote different polarization configurations, where e_i and e_s represent the polarization of the incident and the scattering light; k_i and k_s indicate the corresponding wave vector direction.

III. RESULTS AND DISCUSSION

Representative HRTEM and selected area electron diffraction (SAED) image of the NWs are shown in Figs. 1(c) and 1(d) (side view on the [11$\bar{2}$0] axis), both of which indicate that the NWs grow along [0001] direction with a high-quality wurtzite phase. Combined with a high-angle annular dark-field (HAADF) image, the energy-dispersive spectrometer (EDS) scan of indium, phosphorus, and arsenic element along the radial direction across the NW is shown in Fig. 1(f), which shows the phosphorus element concentrates in the core region of the NWs and the arsenic element concentrates in the shell region. Figure 1(g), a typical SEM image, shows the NWs having a hexagonal cross section with a diameter of 130 nm; thus, the thickness of the core and the shell are about 100 and 15 nm, respectively.

Significant strain is expected in single core-shell NW due to a 3.2% lattice mismatch between the InP core and the InAs shell [29]. We probe the strain of material by measuring the phonon shift of transverse optical (TO) phonon and longitudinal optical (LO) phonon according to the theory of phonon deformation potential [30]. Raman spectroscopy was employed in a backscattering fashion from the [11$\bar{2}$0] facet on NWs under $x(zz)\bar{x}$ and $x(yz)\bar{x}$ polarization configurations using an excitation wavelength of 785 nm. Under such polarization configurations, the excitation of LO modes of InP and InAs is prohibited by the Raman selection rules in Table I. Figure 2(a) shows the Raman spectroscopy of the single core-shell NWs, and only the optical phonon modes of the InP core are identified. The Raman peak at 297.4 cm^{-1} under $x(zz)\bar{x}$ configuration belongs to the A_1 (TO) mode corresponding to atomic vibrations along with the [0001] direction, and the peak at 297.9 cm^{-1} under $x(yz)\bar{x}$ configuration belongs to the E_1 (TO) mode, corresponding to atomic vibrations perpendicular to the [0001] direction. We investigated more than 20 single NWs and recorded consistent spectral differences between A_1(TO) and E_1(TO). Interestingly, the prohibited LO mode appears at 341.4 cm^{-1} due to a resonant effect between the $E_0 + \Delta_0$ energy level of wurtzite InP and the excitation energy (785 nm, 1.58 eV) [31], which breaks the Raman selection rules. In III–V semiconductor NWs, some prohibited LO modes can usually be observed owe to resonance effects [32,33].

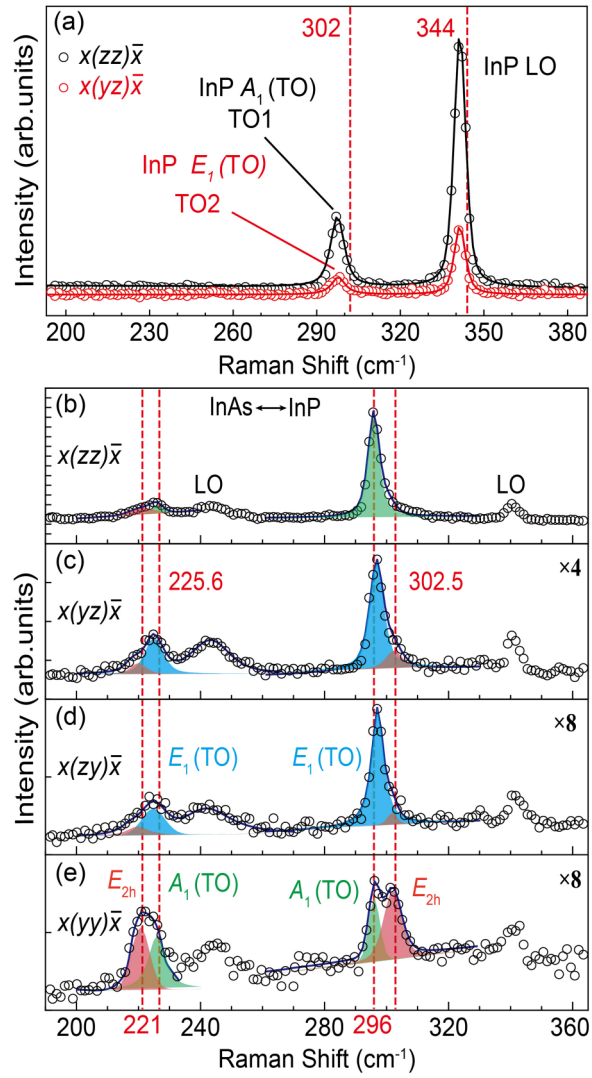

FIG. 2. (a) Raman spectra of single InP-InAs core-shell NW for $x(zz)\bar{x}$ (black circle) and $x(yz)\bar{x}$ (red circle) under the excitation energy of 1.58 eV, and Voigt curves are fitted to the data. TO1 and TO2 represent InP A_1 (TO) under the $x(zz)\bar{x}$ and InP E_1 (TO) under the $x(yz)\bar{x}$, respectively. The Raman frequencies of TO and LO mode of unstrained wurtzite InP are labeled in red dashed line as 302 and 344 cm^{-1}, respectively. (b) Raman spectra from single InP-InAs core-shell NW under different polarization configurations: $x(zz)\bar{x}$, $x(yz)\bar{x}$, $x(zy)\bar{x}$, and $x(yy)\bar{x}$, respectively. The prominent Raman peaks of InAs and InP are in the range of 210–250 and 290–350 cm^{-1}, respectively. The A_1 (TO) and E_{2h} mode of InAs locate at 225.6 and 221 cm^{-1}, and the A_1 (TO) and E_{2h} mode of InP located at 296 and 302.5 cm^{-1} are marked in red dashed line, respectively.

The red dashed lines in Fig. 2(a) denote the Raman frequencies of TO and LO phonon modes of unstrained wurtzite InP at 302 cm^{-1} and 344 cm^{-1} [34,35], respectively. The core-shell NWs, by contrast, show a distinct redshift of InP TO and LO phonon modes toward lower frequency by 4.6 and 2.6 cm^{-1}, respectively, indicating high tensile strain exists in the InP core [36]. Tensile strain plays an essential role in band-gap modulation [37], ferromagnetism modulation [38], and light emission enhancement [39]. Monitoring and controlling

TABLE II. Raman frequencies of measured TO1, TO2, and LO of the InP core and their corresponding strain for three InP-InAs core-shell NWs.

Sample	Measured TO1 (cm^{-1})	Measured TO2 (cm^{-1})	ε_{xx} (%)	ε_{zz} (%)	Measured LO (cm^{-1})	Predicted LO (cm^{-1})
NW 1	297.4	297.9	0.17	0.64	341.4	339.6
NW 2	296.7	297.3	0.19	0.75	340.9	338.9
NW 3	295.8	296.4	0.26	0.81	339.4	338.1

strain in materials offer significant guidance for applications in photonics and electronics.

To calculate the InP core's strain tensor from Raman scattering, we assumed the principal strain to be constant under any rotation from the [0001] direction due to crystal symmetry and is independent of spatial position. The shear components of strain tensor are negligible in wurtzite core-shell NWs because the (0001) atomic planes are flat and symmetric at [0001] direction in the wurtzite core-shell NW heterostructure [40]. Therefore, the strain tensor in Cartesian coordinates is expressed as

$$\varepsilon = \begin{pmatrix} \varepsilon_{xx} & & \\ & \varepsilon_{xx} & \\ & & \varepsilon_{zz} \end{pmatrix}, \tag{1}$$

where ε_{xx} and ε_{zz} are the diagonal components of the strain tensor. For simplicity, we set $\varepsilon_{\mathrm{xx}}$ equal to ε_{yy} due to the geometric symmetry of the core-shell NWs.

We solve the secular equation of phonons by using the shifts of phonon frequency and the phonon deformation potentials [41,42] (PDPs) that describe the response of phonon frequency to stress presented in the crystal. The symmetry of the crystal determines the degeneracy of PDPs. To simplify calculations, we substituted the PDPs of the T_2 mode in zinc-blende structure for the A_1 and E_1 modes in the wurtzite structure because the phonon dispersion along with the [0001] direction (Γ-A path of the Brillouin zone) in the wurtzite phase can be approximated by folding the phonon dispersion along the [111] direction (Γ-L path of the Brillouin zone) in zinc-blende phase for InP [43]. The secular equation of phonons is expressed as the following:

$$\omega_{\mathrm{TO1}}^2 = \omega_{\mathrm{TO}}^2 + (p_{\mathrm{TO}} + q_{\mathrm{TO}})\varepsilon_{xx} + q_{\mathrm{TO}}\varepsilon_{zz}, \tag{2}$$

$$\omega_{\mathrm{TO2}}^2 = \omega_{\mathrm{TO}}^2 + 2q_{\mathrm{TO}}\varepsilon_{xx} + p_{\mathrm{TO}}\varepsilon_{zz}, \tag{3}$$

$$\omega_{\mathrm{LO1}}^2 = \omega_{\mathrm{LO}}^2 + (p_{\mathrm{LO}} + q_{\mathrm{LO}})\varepsilon_{xx} + q_{\mathrm{LO}}\varepsilon_{zz}, \tag{4}$$

where ω_{TO1}, ω_{TO2}, and ω_{LO1} are the phonon frequencies of strained InP; ω_{TO} and ω_{LO} are the phonon frequencies of unstrained InP; p and q refer to different PDPs; TO1 and TO2 represent A_1 (TO) and E_1 (TO) mode of wurtzite InP, respectively. The values of PDPs of the InP [42],

$$p_{\mathrm{TO}} = -2.5{w_{\mathrm{TO}}}^2, \quad q_{\mathrm{TO}} = -3.2{w_{\mathrm{TO}}}^2,$$
$$p_{\mathrm{LO}} = -1.6{w_{\mathrm{LO}}}^2, \quad q_{\mathrm{LO}} = -2.8{w_{\mathrm{LO}}}^2,$$

are applied to Eqs. (2)–(4). The PDPs values used for TO and LO are different due to the energy discrepancy between the TO and LO mode in polar semiconductor [44]. $\varepsilon_{xx} = 0.17\%$ and $\varepsilon_{zz} = 0.64\%$ are obtained, which indicates the InP core exhibits a considerable tensile strain due to the smaller lattice constant of InP relative to InAs [29]. Taking $\varepsilon_{xx} = 0.17\%$ and $\varepsilon_{zz} = 0.64\%$ into Eq. (4), the phonon frequency of the LO mode is calculated to be 339.6 cm^{-1}, which coincides nicely with the measured value of 341.4 cm^{-1}. This proves that the previous approximations and assumptions are reasonable. We show the calculated results of three different NWs in Table II, which indicates that axial strain ε_{zz} is the domination factor for frequency shift of optical phonon mode, agreeing well with our previous calculation [40]. The increase of redshift of the LO phonon from NW1 to NW3 indicates more tensile strain in the InP core, which accords well with our calculation that ε_{zz} increases. Also, the blueshift of phonon frequency [45] in InAs [see Fig. 4(b)] indicates the InAs shell suffers compressive strain due to a larger lattice constant than InP. However, the strain varies considerably from the outer surface to the inner surface of the InAs shell [46]. Thus, it is difficult to achieve a perfect agreement for the InAs shell between measurement and theoretical calculation. (See Supplemental Material [47] for a more detailed discussion.)

Polarization-dependent Raman spectroscopy is a powerful tool to explore the symmetry of phonon modes in a material, which helps identify materials' crystal structure and orientation. The optical phonon modes of wurtzite InP overlap and are difficult to distinguish in ordinary Raman spectroscopy. Therefore, it is necessary to acquire polarization dependence of the optical phonon modes using polarized Raman spectroscopy to understand InP phonons. Figure 2(b) shows characteristic Raman spectra of a single core-shell InP-InAs NW with an excitation wavelength of 632.8 nm under four representative polarization configurations: $x(zz)\bar{x}$, $x(yz)\bar{x}$, $x(zy)\bar{x}$, and $x(yy)\bar{x}$. All the spectra are fitted with the Voigt line-shape function. Each Raman peak is considered a convolution of a Lorentzian and a Gaussian line shape representing intrinsic phonon mode and instrumental response.

Figures 2(b)–2(e) shows that the prominent Raman peaks of the wurtzite InAs shell are in the spectral range of 210–250 cm^{-1}, while the prominent Raman peaks of the wurtzite InP core are in the spectral range of 290–350 cm^{-1}. Three typical phonon vibration modes: A_1 (TO), E_1 (TO), and E_{2h} mode, of both the InP core and the InAs shell are identified under four polarization configurations. For discussion convenience, we firstly investigate the Raman peaks of the InP core. According to Table I, $x(zz)\bar{x}$ polarization configuration allows the A_1 (TO) mode, while $x(yy)\bar{x}$ configuration allows both the A_1 (TO) and the E_{2h} mode. Therefore, the Raman peak located at 296 cm^{-1} filled in the green shade under $x(zz)\bar{x}$ and $x(yy)\bar{x}$ configurations is attributed to the A_1 (TO) mode, and the peak located at 302.5 cm^{-1} filled in the red shade under $x(yy)\bar{x}$ configuration is ascribed to E_{2h} mode. The weak

shoulder appearing at 302.5 cm^{-1} filled in the red shade in $x(yz)\bar{x}$ and $x(zy)\bar{x}$ configurations is assigned to the E_{2h} mode because the same Raman frequency is also observed in $x(yy)\bar{x}$ configuration. The E_{2h} mode originates in the wurtzite phase along with the [0001] direction and can serve as a fingerprint to distinguish a wurtzite phase from a zinc-blende phase. The Raman peak at 296.5 cm^{-1} filled in the blue shade in $x(yz)\bar{x}$ and $x(zy)\bar{x}$ configurations is attributed to the E_1 (TO) mode of InP according to the Raman selection rules in Table I. The E_1 (TO) mode frequency is close to the A_1(TO) mode, which is difficult to distinguish in ordinary Raman spectroscopy measurement. Using polarized Raman spectroscopy, A_1 (TO) and E_1 (TO) modes of InP are identified clearly and easily: A_1(TO) dominate in $x(zz)\bar{x}$ and $x(yy)\bar{x}$ configurations; E_1 (TO) dominate in $x(yz)\bar{x}$ and $x(zy)\bar{x}$ configurations.

Compared to the wurtzite InP, the intensity of the Raman spectra of InAs is weaker. According to Raman selection rules in Table I, the Raman peak at 225.6 cm^{-1} filled in the green shade in $x(zz)\bar{x}$ configuration is attributed to the A_1 (TO) mode of InAs, while the Raman peak at 225 cm^{-1} filled in the blue shade in both the $x(yz)\bar{x}$ and $x(zy)\bar{x}$ configuration is assigned to the E_1 (TO) mode of InAs. The optical mode of InAs is significantly blueshifted relative to 217.5 cm^{-1} of unstrained InAs [45], further indicating the existence of compressive strain in InAs. The broad peak of the InAs observed in $x(yy)\bar{x}$ configuration consists of the E_{2h} mode at 221 cm^{-1} filled in the red shade and the A_1 (TO) filled in the green shade. All the Raman peaks of the InAs shell show a significant blueshift due to the compressive strain resulted from the lattice mismatch between the InAs shell and the InP core. The LO modes of both InAs and InP should be prohibited according to the Raman selection rules, but they both appear in all polarization configurations. We attributed LO modes to the resonance effect between the excitation energy and the band structure of the wurtzite InAs and InP. To uncover the mechanism behind this, we performed a resonant Raman spectroscopy study on the single NW.

We compared the Raman spectra of single NWs excited with different photon energy under the same power in Fig. 3. We first discuss the case of InP. Figure 3(a) shows the intensity of TO [refer to A_1 (TO)] and LO mode of InP under $x(zz)\bar{x}$ increases significantly with decreasing excitation energy. Compared to the intensity of InP TO phonon under excitation energy of 2.33 eV, the Raman signal of the InP TO indicated in green shade excited by the 1.96 and 1.58 eV excitation energy increases by a factor of 5 and a factor of 10, respectively. Remarkably, the TO+LO and the 2LO mode of InP emerge under the 1.96 eV excitation energy and the intensity of the 2LO mode increases sharply under the 1.58 eV excitation energy. The dramatic rise in intensity of optical phonon mode is because the excitation energy, especially the 1.58 eV, is close to the $E_0 + \Delta_0$ energy level (1.53 ∼ 1.58 eV) [31] of wurtzite InP, which indicates a Γ_{7c}-Γ_{6v} transition, involving the split-off valence band due to the spin-orbit coupling, occurs at the center of the Brillouin zone. Under excitation energy of 1.96 and 1.58 eV, the ratio of the Raman peak intensity between the LO and TO mode of InP increases from 0.2 to 5. This indicates LO mode of InP is more sensitive to the resonance effect between excitation energy of 1.58 eV and the $E_0 + \Delta_0$ energy level. Compared to the $x(zz)\bar{x}$

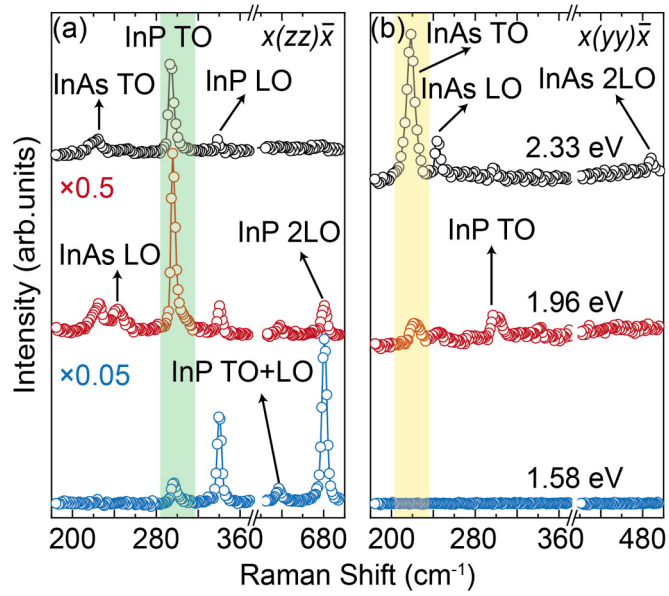

FIG. 3. Raman spectra of a single core-shell NW excited by three excitation energies: 1.58, 1.96, and 2.33 eV, respectively, under the (a) $x(yy)\bar{x}$ and (b) $x(zz)\bar{x}$ configurations.

configuration, the Raman peak intensity in InP core is relatively weak under $x(yy)\bar{x}$ configuration. This is because the resonance of excitation energy with $E_0 + \Delta_0$ energy level depends on the incident light's polarization. For InAs, the Raman spectra of the InAs are alike for excitation energy of 1.96 and 1.58 eV under the $x(yy)\bar{x}$ and $x(zz)\bar{x}$ configurations. However, the intensity of TO mode of InAs indicated in yellow shade increases significantly for the 2.33 eV excitation energy under $x(yy)\bar{x}$ configuration, for which the 2LO mode of InAs appears. The above observed spectral features can be attributed to the resonant effect between the excitation energy of 2.33 eV and the E_1 energy level (∼2.41 eV) of wurtzite InAs [48]. The E_1 energy level represents the electronic band-gap transition occurring along [0001] directions of the Brillouin zone in wurtzite and zinc-blende semiconductors.

To further explore the resonant properties of the core-shell NWs, we studied the azimuthal dependence of the A_1 (TO) mode of InAs and InP on the same NW with two excitation energies, 1.96 and 2.33 eV, respectively. As shown in Fig. 4, the polarization of scattering light is selected to be either perpendicular ($I_\perp$) or parallel ($I_{||}$) to the long axis of the NW, and the polarization of incident light rotates at an angle θ with respect to the long axis of NW. Therefore, the related polarization configurations are expressed as $x(\theta, y)\bar{x}$ and $x(\theta, z)\bar{x}$. For the excitation energy of 1.96 eV, the InAs A_1 (TO) mode predominates in the $x(zz)\bar{x}$ and $x(yy)\bar{x}$ configuration [refer to $x(0, z)\bar{x}$ and $x(90, y)\bar{x}$, respectively]. With increasing excitation energy from 1.96 to 2.33 eV, the intensity of InAs A_1 (TO) phonon mode under $x(yy)\bar{x}$ configuration rises significantly by fivefold. This is due to the resonance between the excitation energy of the 2.33 eV and E_1 gap and shows that the resonance of the InAs A_1 (TO) phonon with excitation light is sensitive to the incident beam's polarization. For InP, the A_1 (TO) mode predominates in the $x(zz)\bar{x}$ configuration for both 1.96 and 2.33 eV excitation energy. The Raman intensity

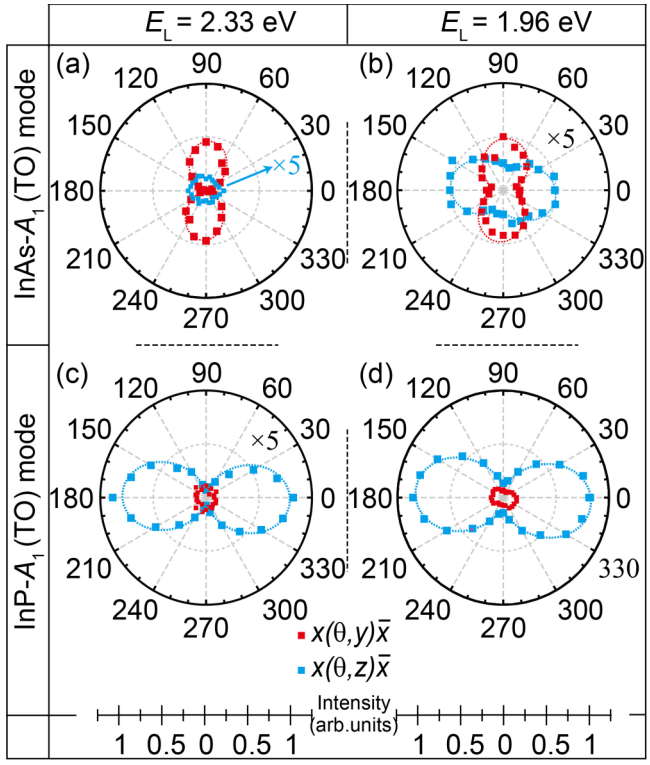

FIG. 4. Azimuthal dependence of the A_1 (TO) modes of the InAs (a), (b) and the InP (c), (d) for 2.33 and 1.96 eV, respectively. The experiment data were marked with squares and fitted with a dashed line. All Raman spectra are normalized to the Raman spectroscopy of InP for the excitation of 1.96 eV under $x(zz)\bar{x}$ polarization configuration.

of InP excited by 1.96 eV photon energy increases fivefold than the Raman intensity excited by 2.33 eV photon energy because the excitation energy of 1.96 eV is in resonance with the $E_0 + \Delta_0$ energy level. The polarization dependence of resonance effect asymmetrically increases the Raman intensity of the optical mode [48], causing the experimental polarization pattern to deviate from the symmetry given by the Raman selection rule in Table I. These findings indicate that resonant Raman spectroscopy with specific polarization is a good way to characterize wurtzite InP and provide significant empirical evidence to explore the electronic band structure of wurtzite InP and InAs.

IV. CONCLUSIONS

We used Raman spectroscopy to investigate the strained state and optical vibration modes of single InP-InAs core-shell NW. Raman spectra show the InP core exhibits tensile strain, and the InAs shell exhibits compressive strain, as expected from the lattice mismatch. Using different polarization excitation configurations, we identified the A_1 (TO), E_1 (TO), and E_{2h} phonon modes in wurtzite InP and InAs. E_{2h} mode appears only in the wurtzite phase and can be regarded as a fingerprint to identify the wurtzite phase from the zinc-blende phase. Using multiple photon energies, the changes in Raman spectra reveal the resonance effect of InP and InAs are related to the $E_0 + \Delta_0$ energy level and the E_1 gap, corresponding to Γ_{7c}-Γ_{6v} transition and electronic band-gap transition occurring along [0001] directions of the Brillouin zone, respectively. The polar patterns show the Raman signal of the A_1 (TO) mode of the InAs core predominant only in the $x(yy)\bar{x}$ polarization configuration, which indicates the resonant effect of InAs A_1 (TO) phonon is sensitive to the polarization of the incident beam. We demonstrate a simple and nondestructive method to characterize the engineered strain in a single core-shell NW structure, which provides a significant guide for predicting and improving the overall performance of the NW arrays. Our findings further deepen the understanding of strain in the InAs and InP of the wurtzite phase under considerable lattice mismatches.

ACKNOWLEDGMENTS

This work was supported by the National Natural Science Foundation of China (Grant No. 11874407), and the Strategic Priority Research Program of Chinese Academy of Sciences (Grant No. XDB 30000000). The authors acknowledge financial support by NanoLund, by the Swedish Research Council, and Myfab.

[1] H. Lee, M. Kim, I. Kim, and H. Lee, Adv. Mater. **28**, 4541 (2016).
[2] L. Zhang, X. Zhong, E. Pavlica, S. Li, A. Klekachev, G. Bratina, T. W. Ebbesen, E. Orgiu, and P. Samorì, Nat. Nanotechnol. **11**, 900 (2016).
[3] Y. Zhou, R. Chen, J. Wang, Y. Huang, M. Li, Y. Xing, J. Duan, J. Chen, J. D. Farrell, H. Q. Xu, and J. Chen, Adv. Mater. **30**, 1802551 (2018).
[4] D. J. O. Göransson, M. Heurlin, B. Dalelkhan, S. Abay, M. E. Messing, V. F. Maisi, M. T. Borgström, and H. Q. Xu, Appl. Phys. Lett. **114**, 053108 (2019).
[5] L. Gao, K. Zeng, J. Guo, C. Ge, J. Du, Y. Zhao, C. Chen, H. Deng, Y. He, H. Song, G. Niu, and J. Tang, Nano Lett. **16**, 7446 (2016).
[6] W. Deng, L. Huang, X. Xu, X. Zhang, X. Jin, S.-T. Lee, and J. Jie, Nano Lett. **17**, 2482 (2017).
[7] A. Fu, H. Gao, P. Petrov, and P. Yang, Nano Lett. **15**, 6909 (2015).
[8] S. Haffouz, K. D. Zeuner, D. Dalacu, P. J. Poole, J. Lapointe, D. Poitras, K. Mnaymneh, X. Wu, M. Couillard, M. Korkusinski, E. Scholl, K. D. Jöns, V. Zwiller, and R. L. Williams, Nano Lett. **18**, 3047 (2018).
[9] M. T. Borgström, V. Zwiller, E. Müller, and A. Imamoglu, Nano Lett. **5**, 1439 (2005).
[10] M. E. Reimer, G. Bulgarini, N. Akopian, M. Hocevar, M. B. Bavinck, M. A. Verheijen, E. P. Bakkers, L. P. Kouwenhoven, and V. Zwiller, Nat. Commun. **3**, 737 (2012).
[11] I. E. Zadeh, A. W. Elshaari, K. D. Jöns, A. Fognini, D. Dalacu, P. J. Poole, M. E. Reimer, and V. Zwiller, Nano Lett. **16**, 2289 (2016).
[12] B. R. Sutherland and E. H. Sargent, Nat. Photonics **10**, 295 (2016).

[13] B. Pal, K. Goto, M. Ikezawa, Y. Masumoto, P. Mohan, J. Motohisa, and T. Fukui, Appl. Phys. Lett. **93**, 073105 (2008).
[14] M. H. Hadj Alouane, R. Anufriev, N. Chauvin, H. Khmissi, K. Naji, B. Ilahi, H. Maaref, G. Patriarche, M. Gendry, and C. Bru-Chevallier, Nanotechnology **22**, 405702 (2011).
[15] Z. Zanolli, M. E. Pistol, L. E. Fröberg, and L. Samuelson, J. Phys.: Condens. Matter **19**, 295219 (2007).
[16] J. W. W. van Tilburg, R. E. Algra, W. G. G. Immink, M. Verheijen, E. P. A. M. Bakkers, and L. P. Kouwenhoven, Semicond. Sci. Technol. **25**, 024011 (2010).
[17] X. Jiang, Q. Xiong, S. Nam, F. Qian, Y. Li, and C. M. Lieber, Nano Lett. **7**, 3214 (2007).
[18] D. J. O. Goransson, M. T. Borgstrom, Y. Q. Huang, M. E. Messing, D. Hessman, I. A. Buyanova, W. M. Chen, and H. Q. Xu, Nano Lett. **19**, 2674 (2019).
[19] S. Lazarev, D. J. O. Göransson, M. Borgström, M. E. Messing, H. Q. Xu, D. Dzhigaev, O. M. Yefanov, S. Bauer, T. Baumbach, R. Feidenhans, L. Samuelson, and I. A. Vartanyants, Nanotechnology **30**, 505703 (2019).
[20] F. Zhou, A. L. Moore, J. Bolinsson, A. Persson, L. Fröberg, M. T. Pettes, H. Kong, L. Rabenberg, P. Caroff, D. A. Stewart, N. Mingo, K. A. Dick, L. Samuelson, H. Linke, and L. Shi, Phys. Rev. B **83**, 205416 (2011).
[21] M. I. Alonso, E. Bailo, M. Garriga, A. Molero, P. O. Vaccaro, A. R. Goñi, A. Ruiz, and M. Alonso, J. Phys. Chem. C **119**, 22154 (2015).
[22] Z. Zhang, D. C. Dillen, E. Tutuc, and E. T. Yu, Nano Lett. **15**, 4303 (2015).
[23] Y. Xiang, I. Zardo, L. Y. Cao, T. Garma, M. Heiß, J. R. Morante, J. Arbiol, M. L. Brongersma, and A. Fontcuberta i Morral, Nanotechnology **21**, 105703 (2010).
[24] S. Yazji, I. Zardo, M. Soini, P. Postorino, A. Fontcuberta i Morral, and G. Abstreiter, Nanotechnology **22**, 325701 (2011).
[25] M. Wang, Y. Gong, F. Alzina, O. Svoboda, B. Ballesteros, C. M. S. Torres, S. Xiao, Z. Zhang, and J. He, Nanoscale **9**, 19328 (2017).
[26] M. Hetzl, M. Kraut, J. Winnerl, L. Francaviglia, M. Döblinger, S. Matich, A. Fontcuberta i Morral, and M. Stutzmann, Nano Lett. **16**, 7098 (2016).
[27] F. Haas, P. Zellekens, T. Wenz, N. Demarina, T. Rieger, M. I. Lepsa, D. Grützmacher, H. Lüth, and T. Schäpers, Nanotechnology **28**, 445202 (2017).
[28] A. Zouitine, A. Ibral, E. Assaid, F. Dujardin, and E. Feddi, Superlattices Microstruct. **109**, 123 (2017).
[29] M. W. Larsson, J. B. Wagner, M. Wallin, P. Håkansson, L. E. Fröberg, L. Samuelson, and L. R. Wallenberg, Nanotechnology **18**, 015504 (2007).
[30] E. Anastassakis, A. Pinczuk, E. Burstein, F. H. Pollak, and M. Cardona, Solid State Commun. **88**, 1053 (1993).
[31] A. De and C. E. Pryor, Phys. Rev. B **81**, 155210 (2010).
[32] M. Möller, M. M. de Lima Jr, A. Cantarero, L. C. O. Dacal, J. R. Madureira, F. Iikawa, T. Chiaramonte, and M. A. Cotta, Phys. Rev. B **84**, 085318 (2011).
[33] I. Zardo, S. Conesa-Boj, F. Peiro, J. R. Morante, J. Arbiol, E. Uccelli, G. Abstreiter, and A. Fontcuberta i Morral, Phys. Rev. B **80**, 245324 (2009).
[34] E. G. Gadret, M. M. de Lima, J. R. Madureira, T. Chiaramonte, M. A. Cotta, F. Iikawa, and A. Cantarero, Appl. Phys. Lett. **102**, 122101 (2013).
[35] J. Chen, G. Conache, M.-E. Pistol, S. M. Gray, M. T. Borgström, H. Xu, H. Q. Xu, L. Samuelson, and U. Håkanson, Nano Lett. **10**, 1280 (2010).
[36] F. J. Lopez, E. R. Hemesath, and L. J. Lauhon, Nano Lett. **9**, 2774 (2009).
[37] B. Wei, K. Zheng, Y. Ji, Y. Zhang, Z. Zhang, and X. Han, Nano Lett. **12**, 4595 (2012).
[38] Y. Zhou, Z. Wang, P. Yang, X. Zu, L. Yang, X. Sun, and F. Gao, ACS Nano **6**, 9727 (2012).
[39] J. R. Jain, A. Hryciw, T. M. Baer, D. A. Miller, M. L. Brongersma, and R. T. Howe, Nat. Photonics **6**, 398 (2012).
[40] F. Boxberg, N. Søndergaard, and H. Q. Xu, Adv. Mater. **24**, 4692 (2012).
[41] F. Cerdeira, C. J. Buchenauer, F. H. Pollak, and M. Cardona, Phys. Rev. B **5**, 580 (1972).
[42] E. Anastassakis, Y. S. Raptis, M. Hunermann, W. Richter, and M. Cardona, Phys. Rev. B **38**, 7702 (1988).
[43] S. Mukhopadhyay and D. A. Stewart, Phys. Rev. B **89**, 054302 (2014).
[44] H. Harima, J. Phys.: Condens. Matter **14**, R967 (2002).
[45] J. K. Panda, A. Roy, A. Chakraborty, I. Dasgupta, E. Hasanu, D. Ercolani, L. Sorba, and M. Gemmi, Phys. Rev. B **92**, 205302 (2015).
[46] M. Montazeri, M. Fickenscher, L. M. Smith, H. E. Jackson, J. Yarrison-Rice, J. H. Kang, Q. Gao, H. H. Tan, C. Jagadish, Y. Guo, J. Zou, M. E. Pistol, and C. E. Pryor, Nano Lett. **10**, 880 (2010).
[47] See Supplemental Material at http://link.aps.org/supplemental/10.1103/PhysRevB.104.235309 for (i) strain in the InAs shell; and (ii) the influence of different shell thickness on the strain.
[48] I. Zardo, S. Yazji, N. Hormann, S. Hertenberger, S. Funk, S. Mangialardo, S. Morkotter, G. Koblmuller, P. Postorino, and G. Abstreiter, Nano Lett. **13**, 3011 (2013).